

## FLOW ENERGY HARVESTING FROM PIEZOELECTRIC FLAGS

**Sébastien Michelin\***

LadHyX – Department of Mechanics  
Ecole polytechnique  
Route de Saclay  
91128 Palaiseau, France

Email: [sebastien.michelin@ladhyx.polytechnique.fr](mailto:sebastien.michelin@ladhyx.polytechnique.fr)

**Olivier Doaré**

Unité de Mécanique (UME)  
ENSTA, ParisTech  
Chemin de la Hunière  
91761 Palaiseau, France

Email: [olivier.doare@ensta-paristech.fr](mailto:olivier.doare@ensta-paristech.fr)

### ABSTRACT

The present work investigates the possibility to produce electrical energy from the flutter oscillations of a flexible plate placed in an axial flow and covered with piezoelectric patches that convert bending and stretching of the plate's surface into electric charge displacement. A fully-coupled nonlinear model for the dynamics of the fluid-solid-electric system is presented and used to determine the influence of the different system parameters on the stability, nonlinear dynamics and energy harvesting efficiency of the system. In particular, the role of the tuning between the fluid-solid and electrical systems is investigated as well as the impact of the flow velocity and fluid-solid mass ratio.

### INTRODUCTION

Global climate change and scarcity of traditional fossil fuels motivate the development of innovative and renewable energy sources with low environmental impact. Converting the kinetic energy associated with geophysical flows such as winds, rivers, oceanic and tidal currents is particularly attractive, given the wide availability of this resource. Classical fluid-solid instabilities such as Vortex-Induced Vibrations, galloping and flutter in axial flows effectively extract energy from the flow and transform it into solid mechanical energy that can then be used to produce electricity using either displacement-based (e.g. electromagnetic converters) or deformation-based energy converters (e.g. piezoelectric materials) [1–5]

In the present work, we are interested in the feasibility and performance of flow energy harvesting using piezoelectric flexible plates, or flags. Thin flexible plates placed in a steady axial flow are known to become unstable to flutter at a critical velocity [6–8], above which

a large amplitude flapping regime can develop, characterized by the propagation of deformation waves along the flag [9]. When a piezoelectric patch is attached on the deforming flag surface, its periodic bending can be converted into electric charge transfers [10]. Use of piezoelectric materials is not adapted to large scale harvesters, but such materials show competitive and promising performances in the domain of small-power devices [11].

Classically, energy harvesting is represented in the fluid-solid system as an additional damping [12], but this approach overlooks the possible coupling between the harvesting circuit and the fluid-solid system powering it. In this study, an explicit description of the harvesting system is introduced in terms of piezoelectric patches, and following Refs. [13, 14], the equations for the fully-coupled fluid-solid-electrical nonlinear dynamics are derived. This approach provides insight on the double impact of energy harvesting, namely producing electrical energy and modifying the behavior of the fluid-solid system. For example, increasing the coupling coefficient might lead to a better energy transfer to the output circuit but could also eventually result in the restabilization of the system due to its damping effect. Considering the model problem of a slender flexible plate in axial flow, we analyze the energy harvesting efficiency of the system in terms of the different fluid-solid-electric parameters.

The present paper is organized as follows: the fluid-solid-electric model is first presented in Section 1. The effect of the piezoelectric coupling on the stability of the system is then analyzed using linear analysis (Section 2). Section 3 finally focuses on the nonlinear dynamics of the system to determine the amplitude and frequency of the saturated flapping motion and assess the energy harvesting efficiency.

---

\*Address all correspondence to this author.

## 1 MODEL

### 1.1 Presentation of the piezoelectric flag

In this work, we consider a rectangular inextensible flexible plate of length  $L$  and span  $l$ , and negligible thickness  $h$ . The plate is clamped at its leading edge and placed in a steady incoming inviscid flow of velocity  $U_\infty$  and density  $\rho$ . The surface of the plate is covered by pairs of piezoelectric patches (one patch on each side) whose negative electrodes have been shunted through the plate and whose positive electrodes are connected to an output resistive circuit (Figure 1). We neglect here any spanwise plate deformation and charge transfer so that the mechanical and electrical state variables are only functions of the streamwise curvilinear coordinate  $s$  and time  $t$ . In the following, for any function  $a(s,t)$ , its derivatives with respect to  $t$  and  $s$  are noted  $\dot{a}$  and  $a_s$ , respectively.

The deformation and position of the cantilevered plate are characterized by the local orientation  $\theta(s,t)$  of the unit tangent vector  $\boldsymbol{\tau}(s,t)$  with the flow direction  $\mathbf{e}_x$ . The difference of potential between the free electrodes on each side of the plate and the charge transfer between those electrodes are respectively noted  $v(s,t)$  and  $q(s,t)$  (Figure 1). In the limit of continuous coverage by patches of infinitesimal length in the streamwise direction [14], the piezoelectric effect results in an additional torque inside the plate imposed by the voltage between the electrodes, namely

$$\mathcal{M}_{\text{piezo}} = -\chi v, \quad (1)$$

with  $\chi$  the piezoelectric coupling, and in a charge transfer  $q$  resulting from the plate's deformation:

$$q = cv + \chi \theta_s \quad (2)$$

with  $c$  the characteristic capacity of the piezoelectric patch pair. Noting  $g$  the lineic conductivity of the output circuit,  $q$  and  $v$  are related through Ohm's law

$$\dot{q} + gv = 0. \quad (3)$$

### 1.2 Non-linear solid dynamics

The system {plate + piezo} is represented as an Euler–Bernoulli beam, and large amplitude displacements of the beam are considered. The beam is inextensible and, taking into account the piezoelectric torque in

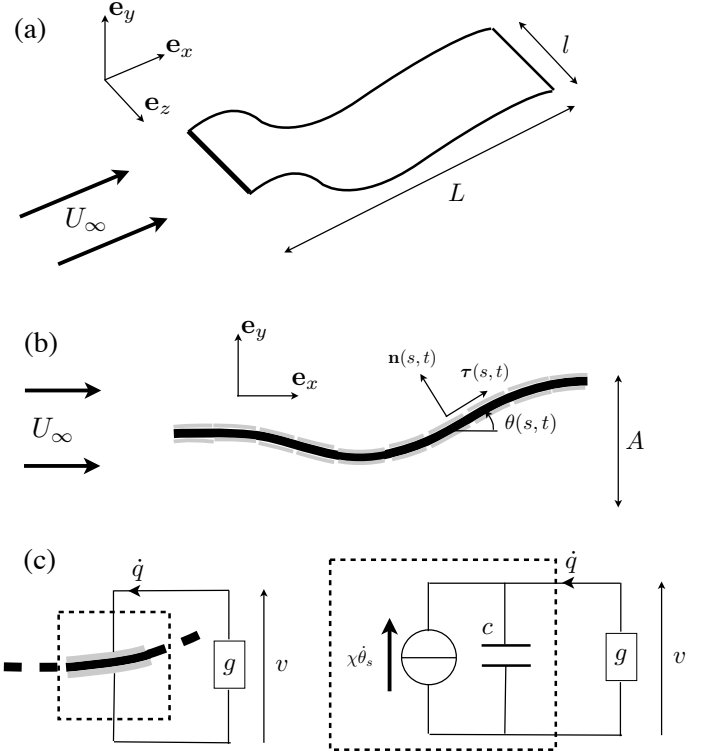


**FIGURE 1:** (a) Two-dimensional motion of a cantilevered slender flexible plate in axial flow. (b) Piezoelectric flag: the flexible plate (black) is covered on each side by piezoelectric patches (grey). (c) each piezoelectric patch pair is connected to a dissipative circuit and the electrical equivalent is given on the right.

Eq. (1), its position  $\mathbf{x}(s,t)$  satisfies

$$\mu \ddot{\mathbf{x}} = \left[ T \boldsymbol{\tau} - (B \theta_{ss} - \chi v) \mathbf{n} \right]_s + \mathbf{f}_{\text{fluid}}, \quad (4)$$

$$\mathbf{x}_s = \boldsymbol{\tau}, \quad (5)$$

where  $B$  and  $\mu$  are respectively the uniform rigidity and lineic mass of the piezoelectric flag,  $T(s,t)$  is the plate's tension and acts as a Lagrangian multiplier to enforce the inextensibility of the plate, and  $\mathbf{f}_{\text{fluid}}$  is the fluid force per unit length on the flag. Clamped-free boundary conditions are used so that

$$\mathbf{x} = 0, \quad \theta = 0 \quad \text{at } s = 0, \quad (6)$$

$$B \theta_s - \chi v = B \theta_{ss} - \chi v_s = 0 \quad \text{at } s = L. \quad (7)$$

### 1.3 Fluid model

We focus here on the slender body limit ( $l \ll L$ ), when the fluid force applied to the plate can be decomposed into two distinct parts: a reactive force [15], resulting from the added inertia of the fluid put in motion by

each cross-section of the plate, and a resistive force [16] accounting for inertial drag and dissipative effects:

$$\mathbf{f}_{\text{fluid}} = -m_a \rho l^2 \left( \dot{u}_n - (u_\tau u_n)_s + \frac{1}{2} u_n^2 \theta_s \right) \mathbf{n} - \frac{1}{2} \rho l c_d |u_n| u_n \mathbf{n}, \quad (8)$$

where  $m_a$  and  $c_d$  are the non-dimensional added mass and drag coefficient associated with the plate's cross-section, respectively, and  $u_\tau \boldsymbol{\tau} + u_n \mathbf{n} = \dot{\mathbf{x}} - U_\infty \mathbf{e}_x$  is the local relative velocity of the solid to the fluid at rest. The validity of this approach, initially developed to evaluate flow forces created by the motion of a fish body in large amplitude deformations, was recently confronted to and found in good agreement with Reynolds-Averaged Numerical Simulations (RANS) at high Reynolds number [17]. Although limited, in theory, to asymptotically small aspect ratios  $l/L$ , it was also shown recently that predictions using this approach provide satisfying results even up to  $O(1)$  aspect ratio [18]. In the following, the aspect ratio is taken as  $H^* = l/L = 0.5$ , and we focus on thin flat plates so that  $m_a = \pi/4$  and  $c_d = 1.8$ .

#### 1.4 Harvesting efficiency

The total power  $\mathcal{P}(t)$  harvested by the system is equal to the energy actually transferred to the output circuit and dissipated in the useful load  $g$ :

$$\mathcal{P}(t) = \int_0^L g v(s,t)^2 ds. \quad (9)$$

The efficiency of the system is defined as the ratio of the harvested energy to the fluid kinetic energy flux through the section occupied by the system:

$$\eta = \frac{\langle \mathcal{P} \rangle}{\frac{1}{2} \rho U_\infty^3 \mathcal{A} l}, \quad (10)$$

with  $\mathcal{A}$  the peak-to-peak flapping amplitude, and  $\langle \mathcal{P} \rangle$  the time-average of the output power.

#### 1.5 Non-dimensional parameters

Equations (1)–(9) are non-dimensionalized using  $L$ ,  $L/U_\infty$  and  $\rho L^3$  as reference length, time and mass, respectively.  $v$  and  $q$  are non-dimensionalized by  $U_\infty \sqrt{\mu/c}$  and  $U_\infty \sqrt{\mu c}$ , respectively. The system is then characterized by five non-dimensional coefficients:

$$M^* = \frac{\rho l L}{\mu}, \quad U^* = U_\infty L \sqrt{\frac{\mu}{B}}, \quad H^* = \frac{l}{L} \quad (11)$$

$$\alpha = \frac{\chi}{\sqrt{Bc}}, \quad \beta = \frac{c U_\infty}{gL}, \quad (12)$$

corresponding to the fluid-solid inertia ratio, the non-dimensional flow velocity, the aspect ratio, the piezoelectric coupling and the tuning of the output circuit, respectively.  $\beta$  is indeed the ratio of the non-dimensional time-scale associated with the output  $RC$ -loop. In the following, all quantities are non-dimensionalized, unless specified otherwise.

## 2 LINEAR STABILITY ANALYSIS

We first consider the impact of the piezoelectric coupling on the linear stability of the flexible plate. In the absence of any coupling ( $\alpha = 0$ ), the plate becomes unstable to flutter for a flow velocity  $U^*$  greater than a threshold value  $U_c^0(M^*)$  [8, 9, 19].

### 2.1 Linearized equations

In the limit of small vertical displacement  $y(s,t)$  of the plate, the linearized equations for  $y$  and  $v$  are obtained from Eqs. (2)–(4) as

$$(1 + m_a M^* H^*) \ddot{y} + 2m_a M^* H^* \dot{y}_s + m_a M^* H^* y_{ss} + \frac{1}{U^{*2}} y_{ssss} - \frac{\alpha}{U^*} v_{ss} = 0, \quad (13)$$

$$\beta \dot{v} + v + \frac{\alpha \beta}{U^*} \dot{y}_{ss} = 0. \quad (14)$$

Assuming  $[y, v] = \text{Re}([Y(s), V(s)]e^{i\omega t})$  with  $\omega$  complex, Eqs (13)–(14), together with the boundary conditions

$$Y(0) = Y_s(0) = 0, \quad (15)$$

$$Y_{ss}(1) - \frac{\alpha}{U^*} V(1) = Y_{ssss}(1) - \frac{\alpha}{U^*} V_s(1) = 0, \quad (16)$$

become an eigenvalue problem for  $[Y, V]$  and  $\omega$ , solved numerically using a collocation method on  $N$  Chebyshev-Gauss-Lobatto points (typically  $N \approx 60$ – $120$ ).

### 2.2 Impact of the piezoelectric coupling on the instability threshold

For a given output circuit (fixed  $\beta$ ), an increase in the piezoelectric coupling  $\alpha$  impacts the dynamics of the system in two ways: (i) it increases the effective rigidity of the system and (ii) it increases the energy transfer to the output circuit where it is dissipated. One therefore expects an increase of the critical velocity (i.e. a stabilization) due to the piezoelectric coupling. In Fig. 2, the critical velocity is represented for increasing values of  $\alpha$ . A stabilization is indeed observed for low  $M^*$  (light fluid or short flag), while a destabilization of the higher

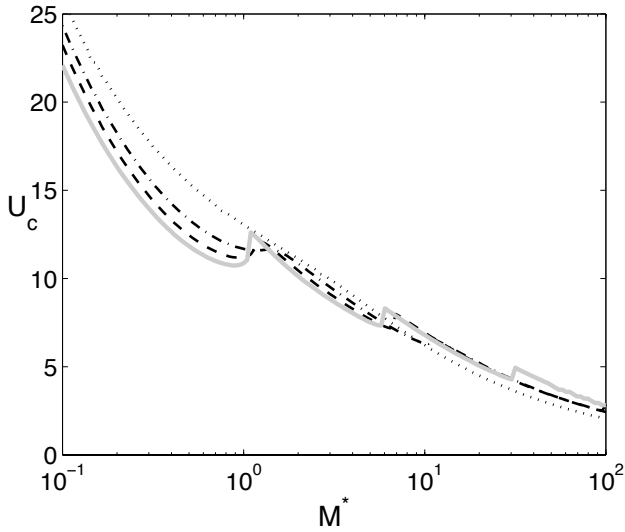


**FIGURE 2:** Critical velocity threshold  $U_c(M^*)$  for  $\beta = 0.1$  and  $\alpha = 0$  (uncoupled, thick light grey),  $\alpha = 0.3$  (dashed),  $\alpha = 0.5$  (dash-dotted) and  $\alpha = 0.9$  (dotted).

order dominant modes is observed for higher  $M^*$  (typically heavier fluid or long flag). This effect was observed recently for a purely two-dimensional model (flag of infinite span), and can be related to the destabilization by damping of negative energy waves in the local stability analysis [14]. One should emphasize that the influence of the piezoelectric coupling is highly dependent on the tuning  $\beta$  of the fluid-solid and electric systems. The results presented in Fig. 2 are obtained when both systems have similar fundamental time-scales.

For a fixed piezoelectric coupling  $\alpha$ , the frequency tuning of the fluid-solid and electrical systems,  $\beta$ , is a measure of the resistance in the output circuit. For  $\beta \ll 1$ , the piezoelectric patches' electrodes are short-circuited: no electric potential is applied to the piezoelectric element and the piezoelectric torque in Eq. (1) vanishes. The flag dynamics is not modified by the piezoelectric, and the critical velocity threshold is that of a flag with no piezoelectric coupling,  $U_c^0$  (Figure 3). On the other hand, when  $\beta \gg 1$ , the conductivity of the output circuit is negligible and no charge transfer can occur between the electrodes. Equations (1)–(2) impose that the potential  $v$ , and therefore  $\mathcal{M}_{\text{piezo}}$  are proportional to curvature and effectively, the piezoelectric coupling acts as an increase in the flag's rigidity. As a result, the critical velocity threshold in this open-circuit limit is obtained directly as  $U_c^0 \sqrt{1 + \alpha^2}$  (Figure 3). Between these two limit cases, the impact described above is recovered: the fluid-solid-electric coupling induces a destabilization of the system at large  $M^*$

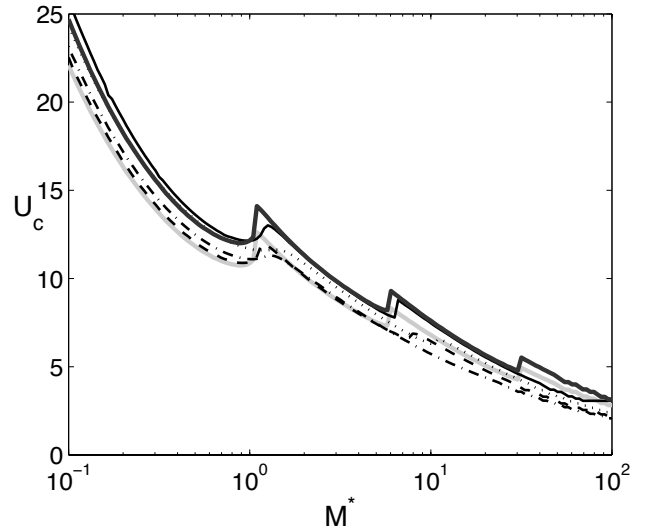


**FIGURE 3:** Critical velocity threshold  $U_c(M^*)$  for  $\alpha = 0.5$  and  $\beta = 0$  (short circuit, thick light grey),  $\beta = 0.1$  (dashed),  $\beta = 0.3$  (dash-dotted),  $\beta = 1$  (dotted),  $\beta = 3$  (solid) and  $\beta = \infty$  (open circuit, thick dark grey)

and a stabilization for small  $M^*$ .

This destabilization by damping is particularly interesting from the point of view of harvesting energy from a flow. In general, the optimal operating regime of the device should be a trade-off between adding enough damping on the system to dissipate energy in the output circuit while maintaining sufficiently high flapping amplitude. When the system is destabilized by damping, initially at least, the addition of damping to the system satisfies both constraints: it increases the energy transfer while maintaining, or possibly enhancing, the flapping dynamics.

### 3 NON-LINEAR DYNAMICS

Studying the nonlinear dynamics of the fully coupled fluid-solid-electric system is necessary in order to determine the characteristics of the limit-cycle oscillations of the system (amplitude and frequency) and assess the amount of power that can be harvested by such a device. The non-dimensional form of Eqs. (1)–(8) is solved numerically using a Chebyshev collocation in space and a second order implicit time-stepping method [20]. The flag is initially at rest, with the piezoelectric patches in their reference configuration ( $q = v = 0$ ). At  $t = 0$ , a small vertical perturbation is added to the horizontal flow to initiate the flag motion.

For  $U^* > U_c$ , the small perturbation results in an exponential growth of the flapping amplitude that eventually saturates (Figure 4). Two different behaviors can

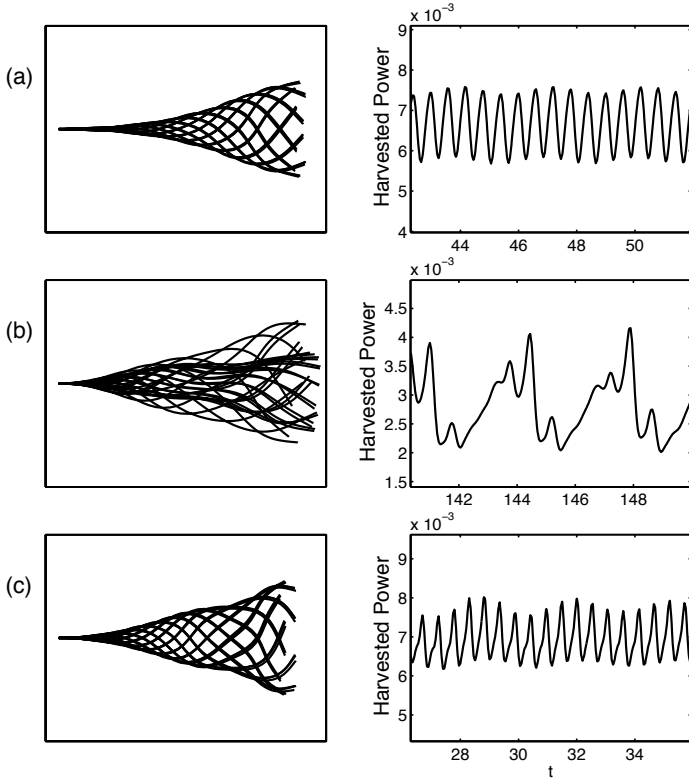


**FIGURE 4:** Flapping dynamics of the piezoelectric flag for  $\alpha = 0.5$ ,  $M^* = 10$ ,  $\beta = 0.158$  and (a)  $U^* = 10.5$ , (b)  $U^* = 11$  and (c)  $U^* = 14.5$ . (Left) Successive position of the piezoelectric flag and (Right) evolution in time of the instantaneous harvested power.

then be observed: (i) the flag enters a strongly periodic regime with a limit cycle oscillation clearly identified or (ii) the flag dynamics is more complex, suggesting some nonlinear interactions between different modes, and some chaotic-looking motion.

A complete discussion of the properties of the latter behavior is beyond the scope of the present work, but it is worth noting that such complex behavior was reported in experimental and numerical studies on the flapping flag dynamics [9, 18, 21, 22], and is not specific to the piezoelectric coupling problem. For fixed  $M^*$ ,  $\alpha$  and  $\beta$ , as  $U^*$  is increased beyond the critical velocity  $U_c$  and more modes become unstable, the system shows different mode switching events, one being illustrated on Figures 4 and 5. The impact of such events on the harvesting performance is important as the amplitude, frequency and curvature distributions are modified.

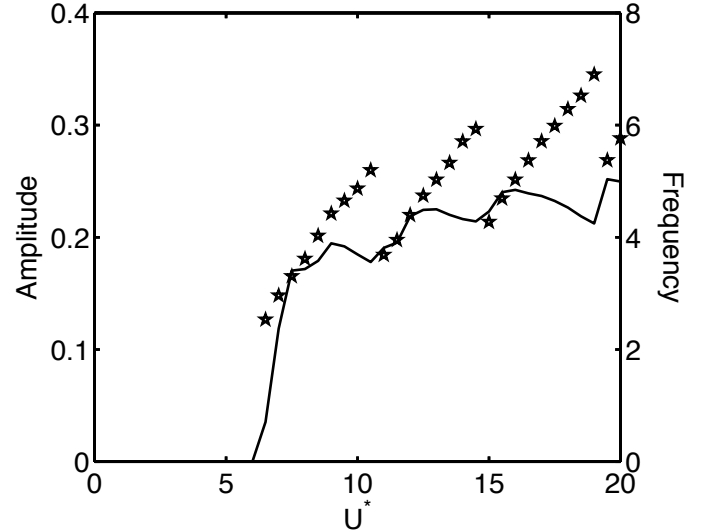


**FIGURE 5:** Evolution with  $U^*$  of the amplitude (solid) and frequency (stars) of the limit-cycle oscillations for  $M^* = 10$ ,  $\alpha = 0.5$  and  $\beta = 0.158$ .

#### 4 HARVESTED ENERGY AND EFFICIENCY OF THE SYSTEM

For a given set of parameters  $(M^*, U^*, \alpha, \beta)$  the dynamics of the piezoelectric system is obtained using the numerical method presented above, and the harvesting efficiency is computed using Eq. (9). When a limit cycle is detected, the efficiency is simply obtained by taking the time-average of  $\mathcal{P}(t)$  over one period, and the non-dimensional flapping amplitude  $A = \mathcal{A}/L$  is computed as

$$A = \sqrt{\langle 2y_e(t)^2 \rangle}, \quad (17)$$

with  $y_e(t)$  the deflection of the trailing edge of the flag.

In the case where a limit cycle can not be identified, the computation is carried over a long enough time frame to ensure that a stationary flapping state has been reached. The efficiency is then obtained using statistical averages over this interval in order to define  $A$  and  $\langle \mathcal{P} \rangle$ .

We are interested here in the influence of the different parameters on the system's performance, measured here by the efficiency  $\eta$ , the ratio of the energy used in the output circuit (i.e. dissipated in the resistive elements) and of the flow kinetic energy flux through the cross-section occupied by the device. In Figure 6, the evolution of  $\eta$  with  $\beta$  and  $U^*$  is represented for two different values of  $M^*$ .

One first observes that  $\eta$  vanishes for both  $\beta \ll 1$  and  $\beta \gg 1$  and is only significant in the intermediate range  $\beta \sim 0.1-1$ , a direct result from the filtering properties of the RC-loop: for  $\beta \ll 1$ , the circuit's resis-

tance is infinitesimal, resulting in negligible energy dissipation despite the charge transfers between the piezoelectric electrodes; for  $\beta \gg 1$ , the resistance is too large for any charge transfer to be possible. The dissipated power is maximum when the frequency of the forcing on the electrical circuit (here, the flapping flag frequency) is close to the circuit's fundamental frequency  $g/c$ . This is confirmed by comparing the results for  $M^* = 1$  and  $M^* = 10$ : for larger  $M^*$ , higher order modes are known to become dominant and have typically higher frequencies [9]. The maximum efficiency is then obtained for a higher characteristic frequency of the electrical circuit, namely a smaller value of  $\beta$  (Figure 6).

For a fixed  $\beta$  and increasing  $U^*$ , successive optimal regions are observed separated by low-efficiency transition regions. This behavior can be interpreted from the mode switching events observed on Figure 4 and 5: as  $U^*$  is increased, the efficiency of the system increases while the dynamics of the system remains locked on the same mode, because the frequency of that mode is increasing with  $U^*$ . However, as more modes become unstable the limit cycle oscillations can lock onto a different mode with lower frequency resulting in a drop in the system's efficiency. One observes that when the fluid inertia is increased (greater  $M^*$ ), mode switching events occur at more closely-spaced values of  $U^*$ .

The effect of  $\beta$  can also be observed on the stability threshold: for small  $M^*$ , the critical velocity increases monotonically with  $\beta$  between the short-circuit and open-circuit limits, while destabilization by damping is observed for larger  $M^*$ . Figure 6(b) also shows that the impact of  $\beta$  on the mode switching thresholds is similar to that on the stability threshold.

The performance of the system can therefore be optimized by tuning the output circuit to the frequency of the flag dynamics. This frequency is however not constant but is itself modified by the fluid-solid-electric coupling. In Fig. 7, we consider the evolution of the efficiency of the optimally-tuned system with  $M^*$  and  $U^*$ : for a given value of these two parameters, the maximum achievable efficiency (over all possible values of  $\beta$ ) is represented. One observes that the efficiency is in general an increasing function of  $U^*$  (as seen previously) and  $M^*$ . This higher efficiency of the high-fluid loading limit (large  $M^*$ ) confirms the linear analysis in Ref. [14], where the energy transfer from the fluid-solid system to the electrical circuit was shown to be more efficient on configurations destabilized by damping. Maximum efficiencies above 10% are achievable, but it must be pointed out that the efficiency is strongly dependent on  $U^*$  at higher  $M^*$  as critical flow velocities leading to mode switching events get closer as

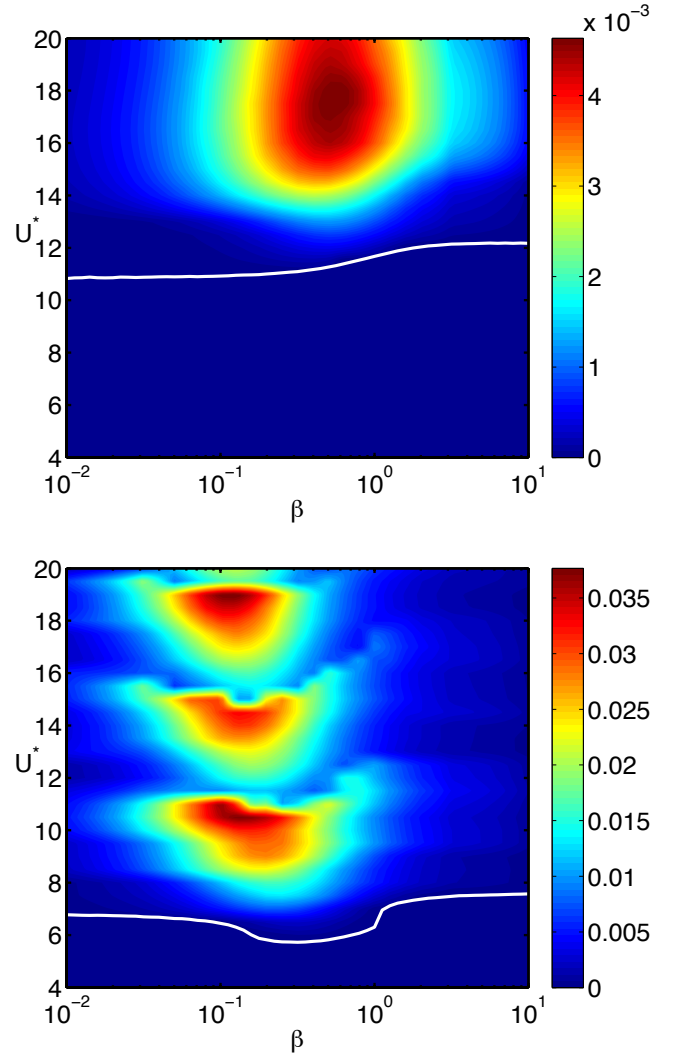


**FIGURE 6:** Evolution of the harvesting efficiency with the tuning ratio  $\beta$  and flow velocity  $U^*$  for  $\alpha = 0.5$  and  $M^* = 1$  (top) and  $M^* = 10$  (bottom). the white line corresponds to the stability threshold.

$M^*$  is increased (Figure 6). This results in an increased sensitivity of the device's performance with the flow velocity.

## CONCLUSIONS

The present study provides some important insight on the coupled dynamics of a classical fluid-solid system (a fluttering flag) and an output circuit producing electrical energy from the deformation of the structure. It was shown that the coupling can lead to a destabilization of the system, corresponding to an increase in the operating range of the device. The destabilized range of fluid loading  $M^*$  also corresponds to the highest harvesting efficiencies. The role of the tuning of the output circuit to

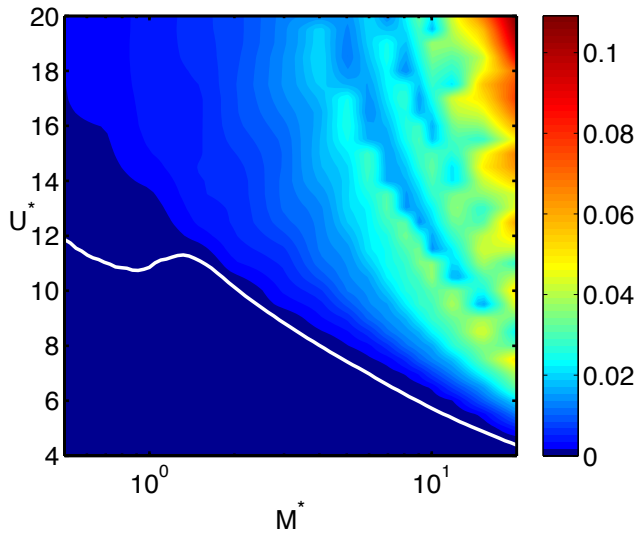


**FIGURE 7:** Optimal energy harvesting efficiency as a function of  $M^*$  and  $U^*$  for  $\alpha = 0.5$ . For each value of  $(M^*, U^*)$ , the maximum efficiency obtained for the optimal value of  $\beta$  is represented. The white line corresponds to the minimum stability threshold over all  $\beta$ .

the fluid-solid frequency is here essential: only carefully-tuned system can harvest a significant amount of energy.

Here, we illustrated the critical role played by the nonlinear flapping mode selection on the energy harvesting efficiency of the system. The locking of the flag on a particular dynamics is a strongly nonlinear phenomenon, and it is expected that it is also influenced by the output circuit behavior. Further investigation is therefore necessary to understand more completely the factors determining the nonlinear dominant mode in order to ensure an increased robustness to the harvesting system with respect to the flow conditions.

#### ACKNOWLEDGMENT

S. M. would like to acknowledge the support of a Marie Curie International Reintegration Grant within the 7th European Community Framework Program.

#### REFERENCES

[1] Bernitsas, M. M., Raghavan, K., Ben-Simon, Y., and Garcia, E. M. H., 2008. “VIVACE (Vortex Induced Vibration Aquatic Clean Energy: a new concept in generation of clean and renewable energy from fluid flow”. *J. Offshore Mech. Arct. Eng.*, **130**, p. 041101.

[2] Barrero-Gil, A., Alonso, G., and Sanz-Andres, A., 2010. “Energy harvesting from transverse gallop-

ing”. *Journal of Sound and Vibration*, **329**(14), pp. 2873–2883.

[3] Peng, Z., and Zhu, Q., 2009. “Energy harvesting through flow-induced oscillations of a foil”. *Phys. Fluids*, **21**, p. 123602.

[4] Singh, K., Michelin, S., and de Langre, E., 2012. “Energy harvesting from axial fluid-elastic instabilities of a cylinder”. *J. Fluids Struct.*, **30**, pp. 159–172.

[5] Grouthier, C., Michelin, S., and de Langre, E., 2012. Energy harvesting using vortex-induced vibrations of tensioned cables. submitted to *J. Fluids Struct.*, preprint available at <http://arxiv.org/abs/1203.0236>.

[6] Paidoussis, M. P., 2004. *Fluid-Structure Interactions, Slender Structures and Axial Flows*, Vol. 2. Academic Press, London.

[7] Shelley, M. J., and Zhang, J., 2011. “Flapping and bending bodies interacting with fluid flows”. *Ann. Rev. Fluid Mech.*, **43**, pp. 449–465.

[8] Eloy, C., Lagrange, R., Souilliez, C., and Schouveiler, L., 2008. “Aeroelastic instability of a flexible plate in a uniform flow”. *J. Fluid Mech.*, **611**, pp. 97–106.

[9] Michelin, S., Llewellyn Smith, S. G., and Glover, B. J., 2008. “Vortex shedding model of a flapping flag”. *J. Fluid Mech.*, **617**, pp. 1–10.

[10] Allen, J. J., and Smits, A. J., 2001. “Energy harvesting eel”. *J. Fluids Struct.*, **15**, pp. 629–640.

[11] Sodano, H., Inman, D., and Park, G., 2004. “A review of power harvesting from vibration using piezoelectric materials”. *The Shock and Vibration Digest*, **36**(3), pp. 197–205.

[12] Tang, L., and Paidoussis, M. P., 2009. “The coupled dynamics of two cantilevered flexible plates in axial flow”. *J. Sound Vib.*, **323**, pp. 214–231.

[13] Bisegna, P., Caruso, G., and Maceri, F., 2006. “Optimized electric networks for vibration damping of piezoactuated beams”. *Journal of Sound and Vibration*, **289**(4-5), pp. 908–937.

[14] Doaré, O., and Michelin, S., 2011. “Piezoelectric coupling in energy-harvesting fluttering flexible plates: linear stability analysis and conversion efficiency”. *J. Fluids Struct.*, **27**, pp. 1357–1375.

[15] Lighthill, M., 1971. “Large-amplitude elongated-body theory of fish locomotion”. *Proc. Roy. Soc. B*, **179**, pp. 125–138.

[16] Taylor, G., 1952. “Analysis of the swimming of long and narrow animals”. *Proc. Roy. Soc. Lon. A*, **214**, pp. 158–183.

[17] Candelier, F., Boyer, F., and Leroyer, A., 2011. “Three-dimensional extension of lighthill’s large-

- amplitude elongated-body theory of fish locomotion". *J. Fluid Mech.*, **674**, pp. 196–226.
- [18] Eloy, C., Kofman, N., and Schouveiler, L., 2012. "The origin of hysteresis in the flag instability". *J. Fluid Mech.*, **691**, pp. 583–593.
- [19] Eloy, C., Souilliez, C., and Schouveiler, L., 2007. "Flutter of a rectangular plate". *J. Fluids Struct.*, **23**, pp. 904–919.
- [20] Alben, S., 2009. "Simulating the dynamics of flexible bodies and vortex sheets". *J. Comp. Phys.*, **228**, pp. 2587–2603.
- [21] Connell, B. S. H., and Yue, D. K. P., 2007. "Flapping dynamics of a flag in uniform stream". *J. Fluid Mech.*, **581**, pp. 33–67.
- [22] Alben, S., and Shelley, M. J., 2008. "Flapping states of a flag in an inviscid fluid: bistability and the transition to chaos". *Phys. Rev. Lett.*, **100**, p. 074301.